Prediction of Van Hove singularity systems in ternary borides

Yang Sun[1,2*†], Zhen Zhang[2†], Andrew P Porter[3,4†], Kirill Kovnir[3,4*], Kai-Ming Ho[2] and Vladimir Antropov[2,4*]

[1]Department of Physics, Xiamen University, Xiamen 361005, China
[2]Department of Physics, Iowa State University, Ames, IA 50011, USA
[3]Department of Chemistry, Iowa State University, Ames, IA 50011, USA
[4]Ames National Laboratory, U.S. Department of Energy, Ames, IA 50011, USA

Abstract

A computational search for stable structures among both α and β phases of ternary ATB_4 borides (A= Mg, Ca, Sr, Ba, Al, Ga, and Zn, T is 3d or 4d transition elements) has been performed. We found that α-ATB_4 compounds with A=Mg, Ca, Al, and T=V, Cr, Mn, Fe, Ni, and Co form a family of structurally stable or almost stable materials. These systems are metallic in non-magnetic states and characterized by the formation of the localized molecular-like state of 3d transition metal atom dimers, which leads to the appearance of numerous Van Hove singularities (VHS) in the electronic spectrum. The closeness of these VHS to the Fermi level can be easily tuned by electron doping. For the atoms in the middle of the 3d row (Cr, Mn, and Fe), these VHS led to magnetic instabilities and new magnetic ground states with a weakly metallic or semiconducting nature. The non-magnetic to magnetic transition can be classified as an example of the Slater transition. Experimental attempts to produce $MgFeB_4$ and associated challenges are discussed, and promising directions for further synthetic studies are formulated.

[†]Equal contribution.
[*]Email: yangsun@xmu.edu.cn (Y.S.); kovnir@iastate.edu (K.K.); antropov@iastate.edu (V.A.)

1 Introduction

2   The electronic density of states (DOS), in the vicinity of the Fermi level E_f ($N(E_f)$), is crucial
3   for the understanding of many properties of metallic systems. A significant $N(E_f)$ value typically
4   leads to a broad spectrum of unusual and exciting electronic, magnetic, and structural properties.
5   However, such large values of $N(E_f)$ simultaneously destroy the stability of the material, creating
6   difficulties in their experimental synthesis. In some cases, losing initial stability is not a destructive
7   factor, as it can transform the system into a stable magnetic, superconducting, or, for instance,
8   charge density state[1–4].

9   A physical reason for developing large $N(E_f)$ was discussed in 1953 when Van Hove
10   demonstrated the crucial role of topology in the electronic or phonon band structure[5]. He has shown
11   that peaks of the DOS are determined by so-called Van Hove critical points or singularities (VHS),
12   i.e., places in the Brillouin zone (BZ), $\boldsymbol{k}$, where (for 2D systems) with energy dispersion $\varepsilon(\boldsymbol{k})$, an
13   ordinary VHS with logarithmically diverging DOS occurs at a saddle point $\boldsymbol{k}$, determined by $\boldsymbol{\nabla_k} = $
14   0. Thus, the energy surface area and the energy-band dispersion are closely related to peaks in the
15   DOS. These VHSs are expected to play an important role in any properties of metallic materials
16   where electrons at the Fermi level are involved.

17   The significance of such VHS becomes stronger in systems with lower dimensions[6–10]. For
18   instance, for 2D materials, the needed VHS is in the middle of the band, where the number of
19   carriers is large. Such VHS 2D materials have been a hot topic in many areas of solid-state physics,
20   especially after discovering high-temperature superconductivity in cuprates [11]. VHS scenario was
21   proposed for the different types of superconductivity, phase separation, magnetic and charge
22   instabilities, and their coexistence [12–14]. Strong effects of VHS have been reported in many other
23   systems. For instance, the anomalies of an anisotropic thermal expansion near points of electronic
24   topological transition (induced by the corresponding VHS) have been discussed in Ref.[15]In general,
25   the effect of the proximity of the Fermi level to VHS on the kinetic and lattice properties of metals
26   and alloys was studied in Ref.[16]. The stress-driven Lifshitz transition was found in Sr_2RuO_4, where
27   the uniaxial pressure lowered the saddle-point singularity below the E_f, which caused enhancement
28   of the superconducting critical temperature [17–19]. Such measurement strongly implies that
29   fermiology plays an ultimate role in mechanisms of many different orderings. For chemical
30   applications, for instance, surface VHS can also serve as a capacitor for the electrons to enhance
31   the contribution of the systems to O_2 absorption through electron transfer[20].

32   This paper presents the results of the density functional-based computational search for stable
33   borides crystallizing in the $YCrB_4$ structural type. We identified α-ATB_4 systems with A=Mg, Ca,
34   Al, and T=V, Cr, Mn, Fe, Ni, and Co as a possible structurally stable family with VHS of different
35   strengths. Below we call these predicted stable systems VHS systems. The strength of these VHS
36   is more pronounced for the atoms in the middle of the 3d row (Cr, Mn, Fe). The change of type of
37   3d atoms represents a convenient way to tune the strength of VHS, which can lead to instability of
38   the paramagnetic Fermi-liquid state of density functional and the formation of a new quantum state.
39   In this paper, we focus on analyzing magnetic instabilities and demonstrate the richness of possible
40   magnetic ground states of these systems. Comprehensive experimental synthetic studies did not
41   yield the desired $MgFeB_4$ phase but allowed us to formulate directions for further synthetic
42   endeavors for ATB_4 systems.

Results and Discussion

Phase stability

45   The 114-type metal borides were first discovered in a series of RE-T-B_4 systems (RE=rare
46   earth, T=transition metals) in the 1970s[21–23]. The 114 families attracted much interest in studying
47   *f*-electron magnetism[24,25]. In the 2000s, the transition metal site in the RE-T-B_4 was doped by Al
48   atoms to form RE-Al-B_4 with heavier and smaller RE elements (RE=Tm, Yb, Lu)[26–29]. $YbAlB_4$
49   stimulated great research interests as the first Yb-based heavy fermion superconductor with
50   quantum criticality[30,31]. It is also predicted to be an ultra-high-temperature ceramic with
51   outstanding thermal and structural properties[32]. While previous studies of 114 systems mainly
52   focused on the properties caused by the RE, the structure is not limited to the RE-based compounds.
53   If the element at A site can form the network to maintain the T dimer and match the (5,7)-
54   membered boron rings, one would expect other stable phases in the 114 structures. However,
55   searching for such candidates can be a heavy burden for direct experimental synthesis.
56   Computational screening with first-principles calculation discovered new materials recently [33–36].
57   Below we perform a computational search for the stable 114 structural systems.

58   114 systems have two polymorphs, i.e., α-phase with the space group *Pbam* and β-phase with
59   the space group *Cmmm*. RE-T-B_4 mainly adopts α-phase while RE-Al-B_4 can have both α and β
60   phases[37]. The structure and properties of α and β phases are usually similar [32]. Figure 1 shows their
61   atomic packing. Both phases consist of a boron layer and a metal layer. The boron layer comprises
62   a combination of (5,7)-membered rings. The metal layer shows a hexagonal framework of larger

63 A atoms. Two smaller T atoms form a dimer in the center of the A framework. Along the out-plain

64 direction, the A site corresponds to the center of the 7-membered ring in the boron layer, while T-

65 site aligns to the center of the 5-membered ring. Intradimer one in the *a-b* plane is the closest

66 distance between the T site atoms (~2.3-2.6 Å). The second nearest distance between the interlayer

67 dimers, along the *c* direction, is ~40% longer than the intradimer distance. The third nearest

68 distance between the dimers is in the plane (>6 Å). Therefore, the intradimer interaction between

69 T atoms is expected to be strongest, while interaction along the *c*-direction should be somewhat

70 weaker. Whether or not T atoms can interact in the plane is to be found. The main difference

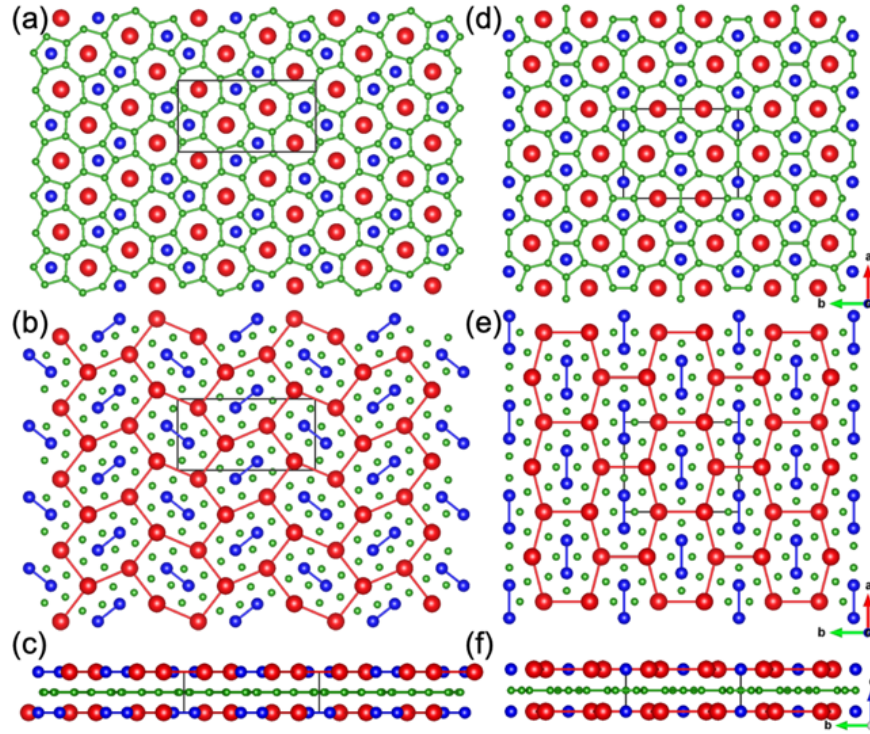71 between α phase and β phase is in the orientation of in-plain networks within the 3d atoms layer.

Figure 1. Crystal structure of (a-c) α-ATB$_4$ and (d-e) β-ATB$_4$. (a, d) The network in the boron layer forms (5,7) rings; (b, e) The network in the metal layer. Metal A forms 6 membered-ring framework, and T forms a dimer. (c, f) Side view of metal and boron layers. Red shows the A site; Blue shows the T site; Green shows B atoms.

78 The computational screening of stable phases was performed on both α and β phases of ATB$_4$.

79 We consider typical *3d* and *4d* transition metal elements for the T site, including V, Cr, Mn, Fe,

80 Co, Ni, Zr, Nb, and Mo. For the A site, we consider Mg, Ca, Sr, Ba, Al, Ga, and Zn, which have

4

81 relatively large ionic radii. Figure 2 shows the energy (E_d) of these ATB$_4$ phases above the convex

82 hull formed by the compounds in existing A-T-B phase diagrams from the Material Project

83 database[38]. We identified two stable phases as new ground states, MgMnB$_4$ and MgFeB$_4$. Phonon

84 calculations confirm that these phases are all dynamically stable (see Supplementary Fig. S1). In

85 addition to the ground states, a lot of low-energy metastable phases can be identified from Fig. 2.

86 If using a criterion of $E_d \sim 0.2$ eV/atom to classify these metastable phases, one can see the stable

87 and metastable phases almost only consist of $3d$ transition metals at T sites, with the A site only

88 occupied by Mg, Ca, or Al. The α phases always show lower energy for these compounds than the

89 β phases, while their energy differences are relatively small (Fig 2). In addition to the two stable

90 phases, the experiments might achieve these metastable phases with $E_d < 0.2$ eV/atom. For

91 instance, the LiNiB compound with $E_d = 0.21$ eV/atom was recently synthesized from high-

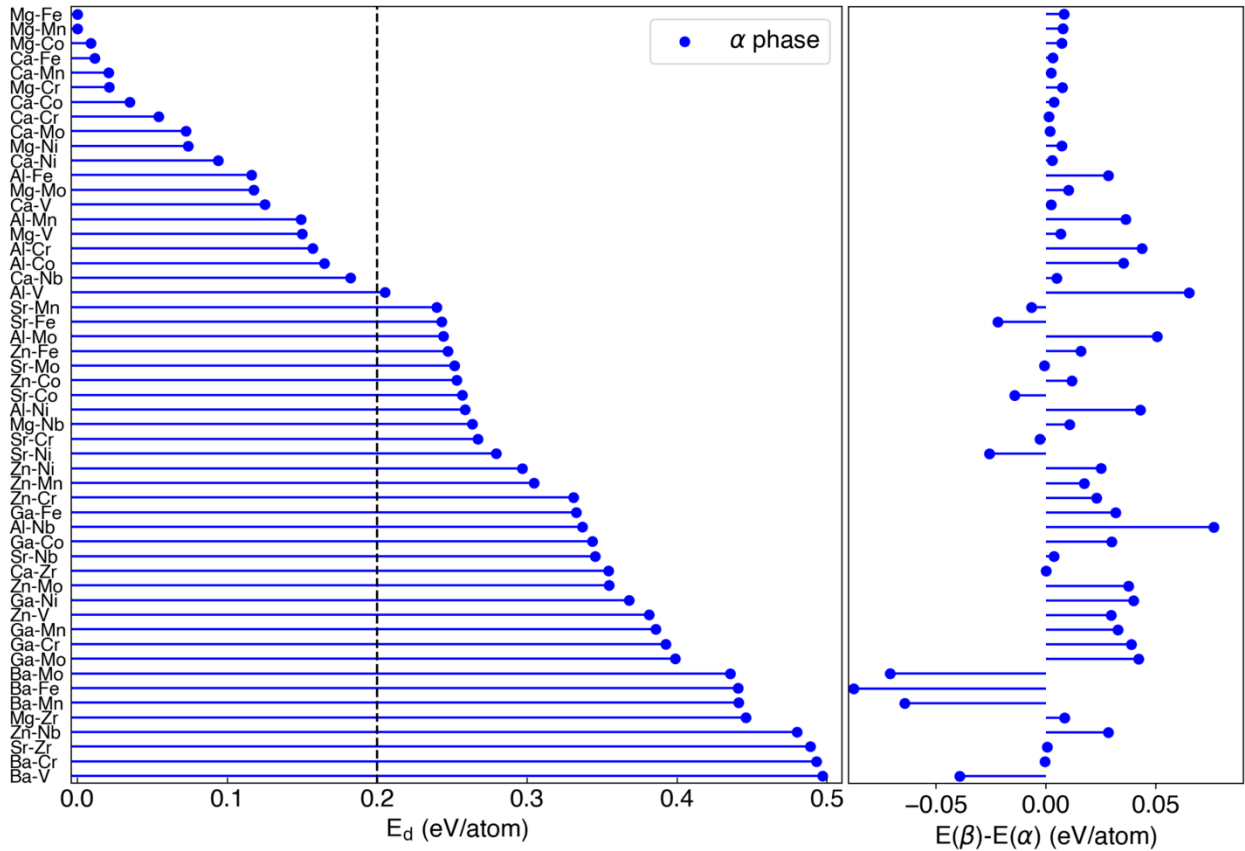92 temperature reactions using the hydride synthetic method [39,40].

93
94 **Figure 2 Stability of non-RE ATB$_4$ phases.** The left panel shows the energy above the convex

95 hull (E_d) for the α phase. The right panel shows the energy difference between β and α phases. The

96 vertical axis labels indicate specific A-T elements combinations. The dashed line indicates the 0.2

97 eV/atom threshold to identify the metastable phases.

Electronic structures

We now focus on stable or metastable α-ATB$_4$ systems: A is Mg, Ca, or Al, and T is V, Cr, Mn, Fe, Ni, or Co. Their non-magnetic (NM) electronic densities of states (DOS) are shown in Fig. 3. First, a significant amount of VHS near the Fermi level can be identified for many systems, especially for the atoms of the middle of the 3d-band (Cr, Mn, Fe), where the number of carriers is large. By comparing the DOS among different compounds, we find a few recurring characters: First, the states near the Fermi level mainly belong to transition metal atoms forming strongly bonding dimers, with a minor contribution from B atoms and almost no contribution from Mg, Ca, or Al atoms. Second, the DOS for the different elements follows rigid band behavior. This is illustrated by Supplementary Fig. S2, which shows the integrated partial DOS for Mn in MgMnB$_4$. When we shift the Fermi level up (or down), imitating the addition (Fe) or removing (Cr) 1 electron, the resulting PDOS is very similar to the actual calculational PDOS for MgFeB$_4$ or MgCrB$_4$, respectively. From Fig. 3, one can also see that when moving from V to Cr systems and further to Mn and Fe, the Fermi level is situated at or near some VHSs. These VHSs are very strong for Cr and Mn atoms, are somewhat weaker for Fe, and are much inefficient for Co, Ni, and V based 114 systems.

When the A site is occupied by Al (right column in Fig. 3), the localized states of transition metals remain; however, relative positions of Fermi levels to the localized peaks are different from the Mg-based or Ca-based compounds in the same row. It is related to the various electronic populations for these systems as Al has one additional valence electron relative to Mg or Ca system. Thus, the DOSs for the discussed family of compounds contain numerous localized dimer states above and below the Fermi level and follow rigid band behavior under doping. This observation can be verified experimentally (pending successful synthesis) as such well-defined localized states of 3d atomic dimers can be seen directly by spectroscopic experiments (optics in particular).
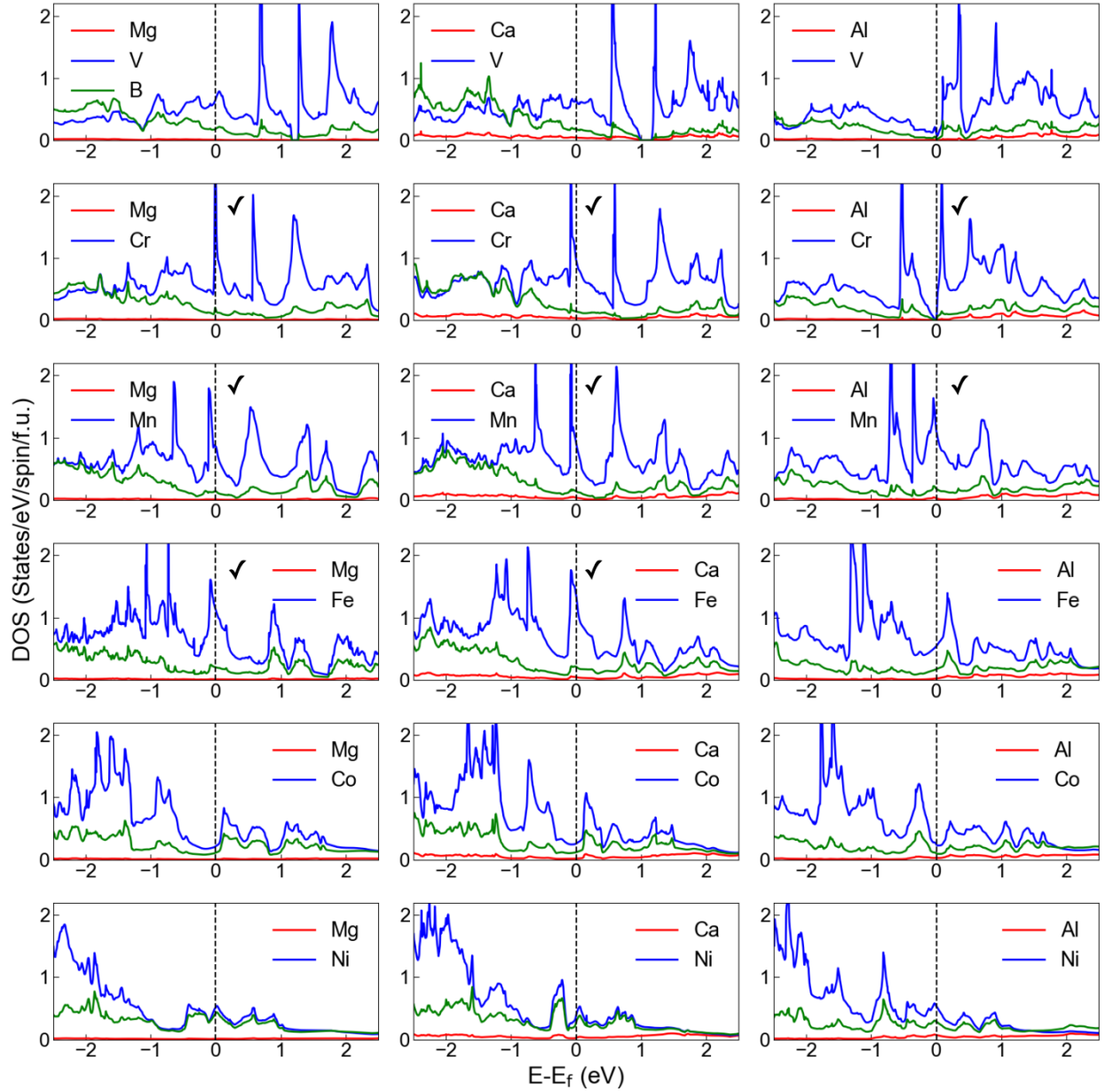
Figure 3 The non-magnetic density of states for α-ATB₄ (A=Mg, Ca, and Al; T=V, Cr, Mn, Fe, Co, Ni). Each column has the same A element, while each row has the same T element. Contributions of states from A (red curve), T (blue curve), and B (green curve) are shown. The tick indicates the systems with a magnetic ground state.

VHS corresponds to the regions of the BZ where flat bands are located. In Fig.4, we show the location of such flat bands for nonmagnetic Mg-based systems. The dispersionless electronic structure at the Z-U-R-T path is persistent in all three compounds. Note Z-U-R-T path is parallel to the layer plane. These flat bands are the manifestation of localized electrons in the planes.

7

According to the projected orbitals on the band structures in Supplementary Fig. S3, these flat bands have dominantly 3d orbital characters of transition metals with a minor contribution from B's p orbital. These localized states correspond to forming quasimolecular isolated dimer states of 3d atoms.
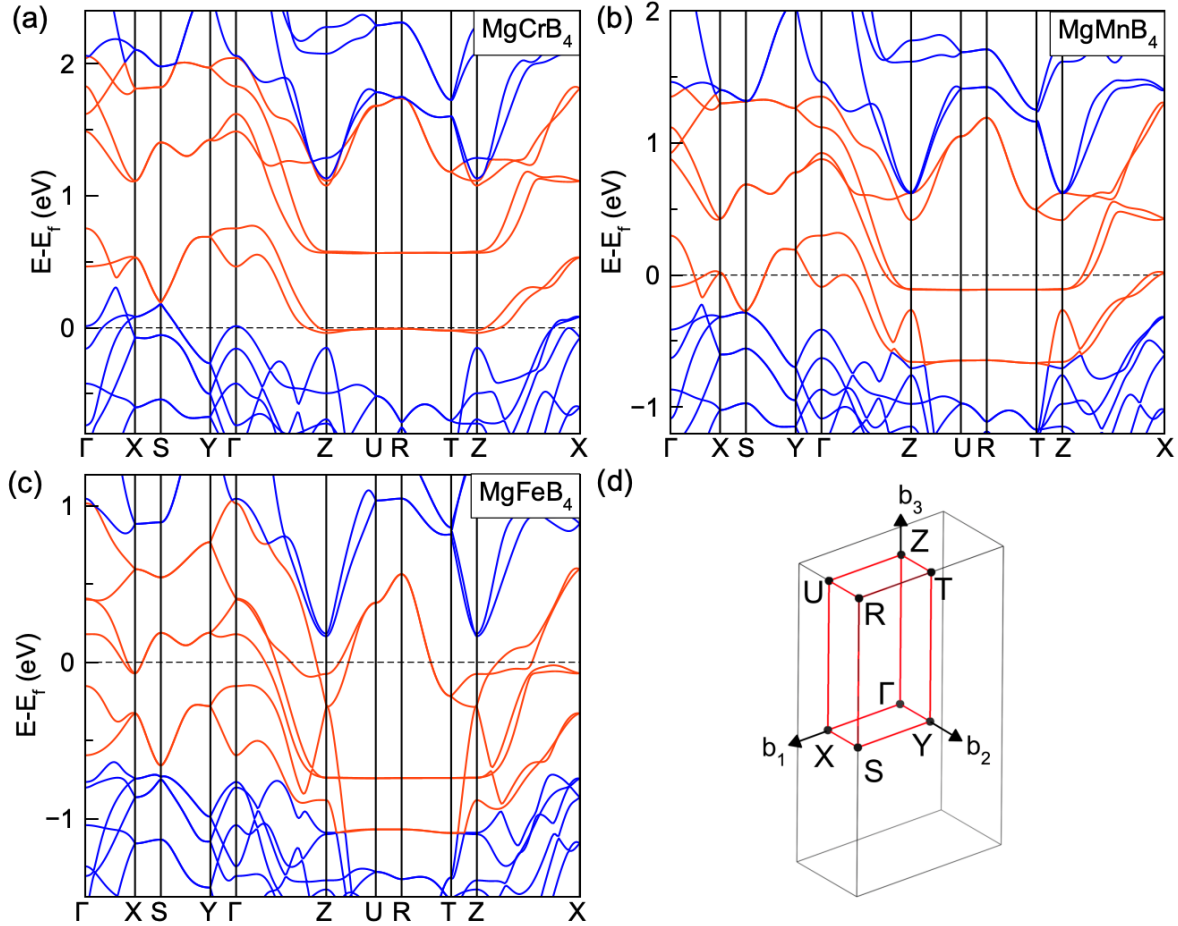

Figure 4 Band structure for non-magnetic MgCrB$_4$, MgMnB$_4$ and MgFeB$_4$. The inset in the left panel shows the bulk Brillouin zone. Red highlights the bands with localized states.

The position of VHS in these systems is only sometimes precisely at the Fermi level in these nonmagnetic calculations. For instance, in AlCrB$_4$, the Fermi level is practically in the gap, while the low $N(E_f)$ can also be seen for Al(V, Fe, Co)B$_4$ and (Mg, Ca)CoB$_4$, though the VHS is close to the Fermi level in all these cases. If the rigid band scenario is valid, one can predict that under suitable hole (electron) doping, one can situate the VHS at the Fermi level and study how the corresponding electronic fluctuations would change the ground state. We will leave this question for future publication and now will switch to the analysis of magnetic instabilities induced by observed VHS in non-magnetic states.

Magnetic states

While, as we discussed earlier, the VHS in the electronic spectrum can lead to many possible instabilities of electronic subsystems, one of them is particularly convenient to study using density functional calculations. This ferromagnetic instability is defined by fulfillment of the Stoner criteria, which indicates that for systems with 3d atoms, if the value of $N_T(E_f)$ is around 1 1/eV, the system is close to such instability. Figure 3 and Table 1 demonstrate that such instability exists in several of our systems. Of course, VHS in DOS can only provide information about FM instability. We must analyze corresponding Fermi-level singularities of spin susceptibility for instabilities in metals induced by all other magnetic orderings. Below we avoid this step by performing a direct self-consistent search of different collinear states.

Table 1 The density of states at the Fermi level of transition metal (T), $N_T(E_f)$ (in states/eV/spin/T), from non-magnetic calculations.

Compounds	$N_T(E_f)$	Compounds	$N_T(E_f)$	Compounds	$N_T(E_f)$
$MgVB_4$	0.667	$CaVB_4$	0.674	$AlVB_4$	0.162
$MgCrB_4$	2.629	$CaCrB_4$	0.979	$AlCrB_4$	0.028
$MgMnB_4$	0.865	$CaMnB_4$	0.945	$AlMnB_4$	1.067
$MgFeB_4$	1.172	$CaFeB_4$	1.227	$AlFeB_4$	0.592
$MgCoB_4$	0.243	$CaCoB_4$	0.302	$AlCoB_4$	0.251
$MgNiB_4$	0.512	$CaNiB_4$	0.351	$AlNiB_4$	0.535

In our 114 structure, one can consider three types of collinear magnetic order between T atoms. To clarify them, we use <**ijk**> notation to represent the magnetic orders, where **i**, **j**, and **k** are either F (ferromagnetic) or A (antiferromagnetic). **i** represents the magnetic order within a dimer between two dimer atoms. **j** represents the magnetic order between two dimers in *a-b* plain, while **k** represents the magnetic order between layers of dimers along the *c* direction. With this notation, there are eight different FM and AFM structures. Figure 5 shows the ground-state magnetic configurations for each magnetic compound with their magnetic energy and corresponding magnetic moments. All other systems do not show stable magnetic ordering with this subset of possible magnetic states. Obtained magnetic ground states of $MgCrB_4$, $MgMnB_4$, and $MgFeB_4$ are different, i.e., <AAA>, <AFF> and <FFA>, respectively. The energy of these states is about 40-80 meV/T lower than the NM state, which is like that of FM fcc Ni (60meV/Ni). The magnetic

172 moments on transition metal atoms are generally close to 1 μ_B (0.6 μ_B in FM fcc Ni). Thus, we

173 expect these magnetic dimers' thermal stability to be very high as the Stoner temperature is

174 expected to be like the one of Ni (>2500K). Ca-based compounds show the same magnetic ground

175 states as Mg-based compounds, suggesting very similar isoelectronic behavior (like the rigid band

176 behavior of DOS discussed earlier). The magnetic behavior of Al systems appears to be similar to

177 both Mg and Ca systems with the corresponding electronic population shifted by +1: $AlCrB_4$ has

178 the same magnetic ground state as (Mg, Ca) MnB_4, and $AlMnB_4$ behaves as (Mg, Ca)FeB_4. The

179 case of $AlCrB_4$ is nontrivial due to the stable antiferromagnetic insulating <AFF> state. Whether

180 or not the non-magnetic and magnetic states of $AlCrB_4$ represent two stable solutions or whether

181 the non-magnetic state possesses unusual magnetic instability will be discussed in future
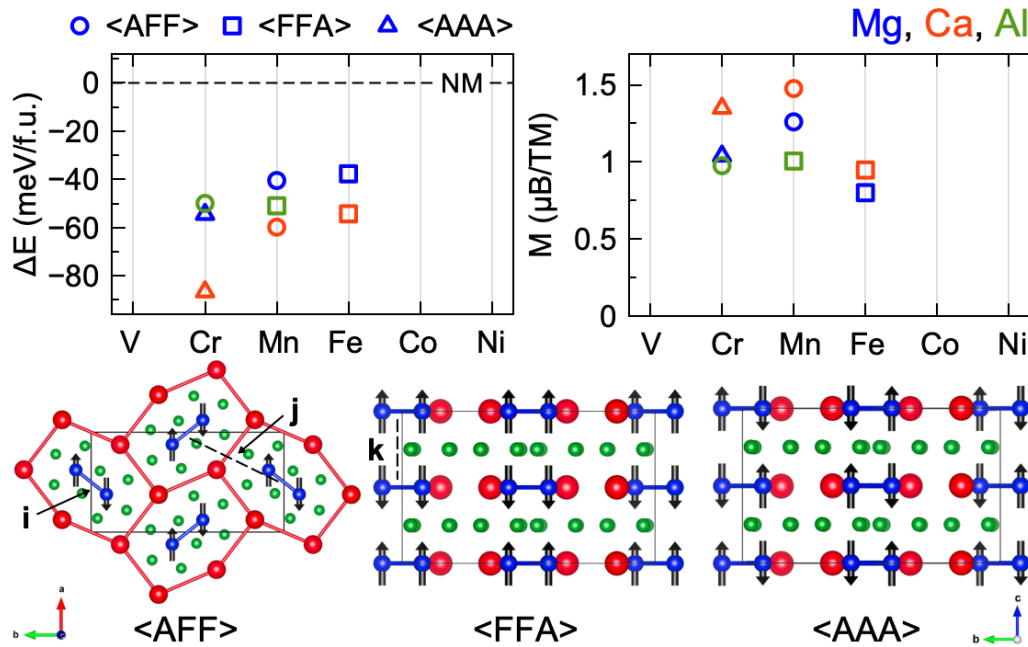
182 publications.

183

184 **Figure 5 The energy difference and magnetic moment for ground states**. The symbols indicate

185 different magnetic orders: circles for AFF, squares for FFA, and triangles for AAA. Different

186 colors show different elements: Mg (blue), Ca (red), and Al (green). The compounds with V, Co,

187 and Ni do not have magnetic solutions.

188   Overall, all nonmagnetic states appear to be metallic, and in the case of Cr and Mn, magnetic

189 interactions of density functional theory drive these metals to insulators. In this sense, the physics

190 appears as the Slater metal-insulator transition proposed more than 70 years ago [41]. However, while

191 the idea is theoretically very attractive, numerous experimental studies claimed that electron-

192 electron interaction is more important for most materials than magnetic interactions. Thus, most

193 known materials with metal-insulator transition follow strongly correlated scenarios or Mott

194 behavior. Systems with Slater's metal-insulator transition are unique, and our prediction must be

195 verified experimentally. The absence of magnetic states for Ni, Co, and V systems is most likely

196 related to the fact that significant VHS near the Fermi level is not formed for the atoms of the

197 beginning and the end of the 3d row.

198   Figure 6 shows the spin-polarized DOS for magnetic ground states in Mg- and Al-based 114

199 compounds. The DOS of Ca-based compounds are like Mg-based compounds, which can be seen

200 by comparing the first column, i.e., <AAA>-MgCrB$_4$ and <AAA>-CaCrB$_4$. Compared to the NM

201 DOS in Fig. 3, the magnetism strongly reduces the $N(E_f)$, stabilizing the new ground state. The

202 obtained ground states all show very low $N(E_f)$ and represent either semiconducting or weekly

203 metallic states. In all cases, fluctuations are suppressed in the newly ordered ground magnetic state.

204 The actual situation can be even more insulating as GGA/LDA methods traditionally tend to

205 produce a metallic state where it does not exist experimentally and underestimate the energy gap

206 in semiconductors. The extended discussion of the locality of the magnetic moments and the

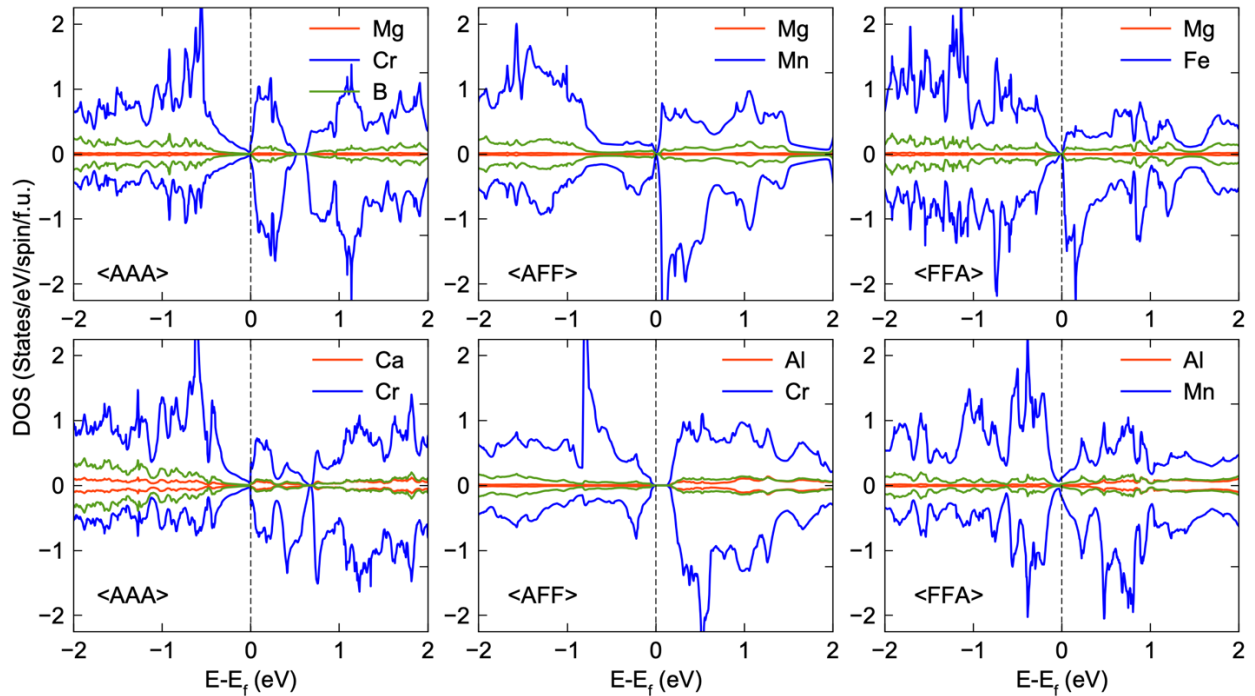207 stability of other magnetic states will be presented in future publications.

208

209 **Figure 6** The spin-polarized density of states for magnetic ground states of <AAA>-MgCrB$_4$,

210 <AFF>-MgMnB$_4$, <FFA>-MgFeB$_4$, <AAA>-CaCrB$_4$, <AFF>-AlCrB$_4$, and <FFA>-AlMnB$_4$.

11

Superconductivity

We also examine the electron-phonon coupling (EPC) strength in the 114 systems, as metal borides can show phonon-mediated superconductivity [42]. We employ a recently developed frozen-phonon method to efficiently screen strong EPC candidates to compute the zone-center EPC strength[43]. This method can identify the strong EPC candidates in MgB_2 and many metal borides because the zone-center EPC strongly correlates with these materials' full Brillouin zone EPC [43,44]. In Fig. 7, we plot the zone-center EPC, λ_Γ, for the non-magnetic states of low-energy α-ATB_4 (A=Mg, Ca and Al; T=V, Cr, Mn, Fe, Co, Ni) compounds. We reference the zone-center EPC of MgB_2 computed in [43]. It shows that all these 114 phases do not possess any strong EPC. Therefore, in these 114 systems, significant electron-phonon superconductivity should not be expected.
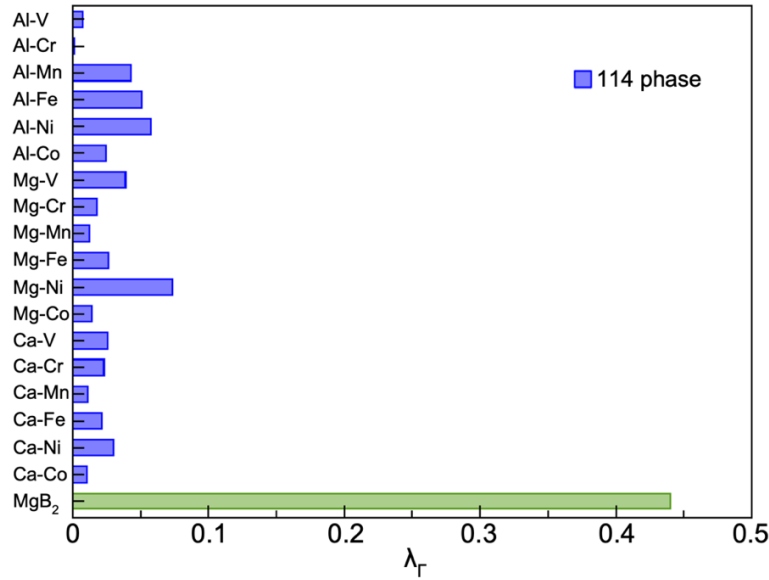

Figure 7. Zone-center EPC strength for non-magnetic α-ATB_4 (A=Mg, Ca, and Al; T=V, Cr, Mn, Fe, Co, Ni). Green is MgB_2 as a reference[43].

However, we cannot dismiss the opportunity of spin fluctuation or plasmon-mediated superconductivity in these systems. While compounds with Cr and Mn can be eliminated from consideration due to the presence of very localized magnetic dimer states, the corresponding Fe (with Al) and all Co and Ni systems indeed represent metallic systems with the average value $N(E_f)$ close to the one in iron pnictides superconductors. The DOSs for all these non-magnetic systems (Fig.3) show certain singularities near the Fermi levels suggesting possible spin fluctuations. It is also evident that the amplitude of these fluctuations in these systems most likely can be tuned by electronic (hole) doping. It is seen from the DOSs of $MgCoB_4$ and $CaCoB_4$ or $AlFeB4$ and $AlCoB_4$

232 (Fig. 3) where significant VHS exist right below and above the Fermi level. The Fermi surface of

233 MgCoB$_4$ is shown in Fig. 8. It forms anisotropic ellipsoids along the c direction, i.e., the ladder

234 direction of spin dimers. Such strong anisotropy in the Fermi surface can accompany

235 superconductivity such as those observed in MgB$_2$ and cuprates [45,46]. Doping in the structure can

236 move the VHS peak closer to the Fermi level, increasing N(E$_f$) by 2-3 times. Thus, one can expect

237 that the amplitude of such fluctuations can be so high that even the novel magnetic state can

238 stabilize. Such tuning of the strength of spin fluctuations near the quantum critical point in these

239 layered boride systems represents a convenient playground for searching for spin fluctuation-

240 mediated superconductivity [47]. We leave the analysis of these fluctuations and their relevance for

241 the superconductivity for future publications.
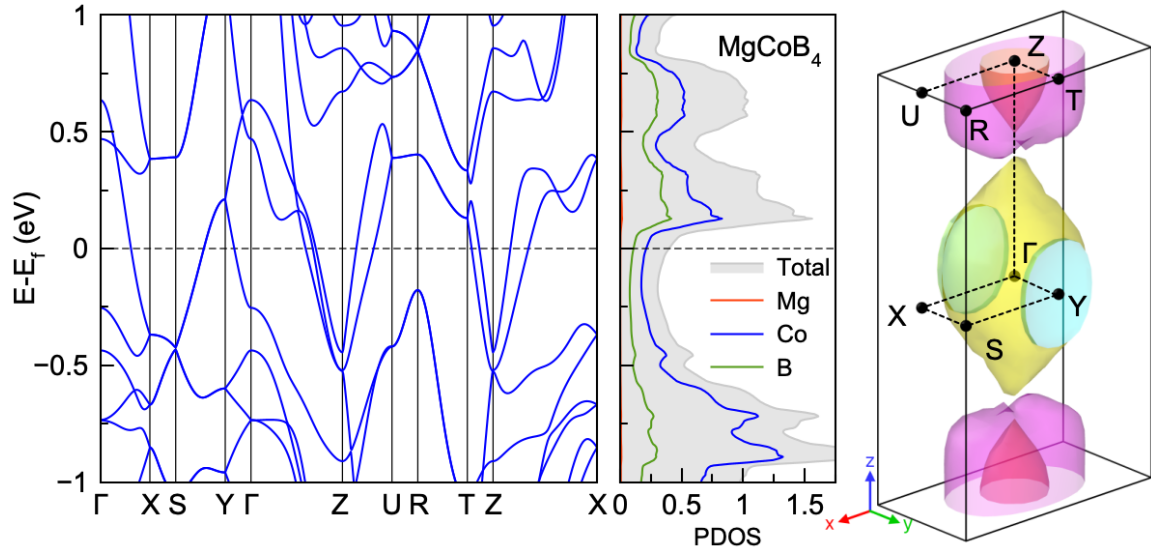

243 Fig. 8 Band structure, density of states, and Fermi surface of MgCoB$_4$.

Synthesis exploration

246   Due to exciting, predicted properties, we focused on the MgFeB$_4$ compound for the synthetic

247 exploration. Several factors make a synthesis of the MgFeB$_4$ phase challenging. Boron is a

248 refractory element that requires a higher temperature to activate. Methods such as arc melting are

249 commonly used to synthesize transition metal borides. In contrast, magnesium is a reactive element

250 with high vapor pressure, T$_{boiling}$ = 1100°C. This reactivity difference precludes using of arc-

251 melting or other high-temperature methods. We have recently shown the power of the mixing of

252 refractory materials method when two refractory components are mixed by forming a binary

253 compound via arc melting. The resulting compound is introduced into a reaction with more active

254 components simultaneously and in close spatial proximity [48–51]. This method cannot be applied to

255 Fe-B mixing due to the absence of boron-rich Fe borides. Melting of Fe+4B resulted in a mixture

256 of FeB+3B, preventing homogeneous Fe-B mixing. The phase diagram shows that Mg and Fe

257 metals are also immiscible [52]. Our preliminary attempts to perform a reaction of elements in a wide

258 temperature range of 600-1000°C were unsuccessful; they all produced a mixture of MgB_2, iron
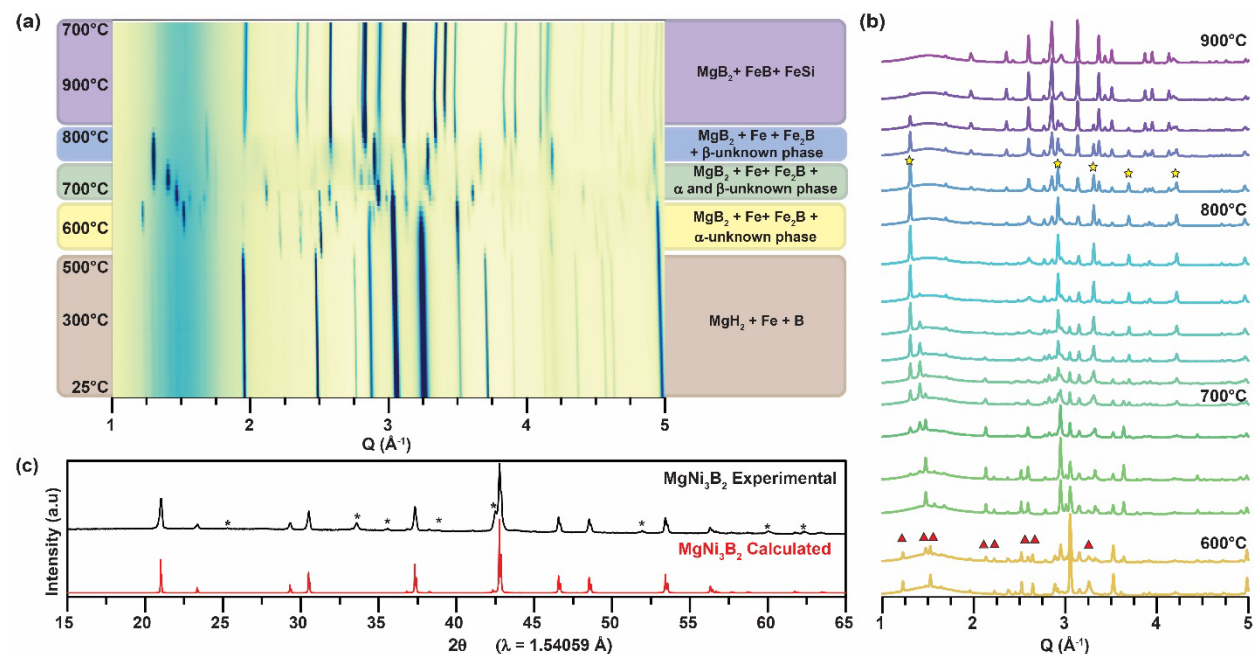
259 borides, and unreacted boron.

261 Fig. 9 (a) In-situ powder X-ray diffraction investigation of the reaction of $1.3MgH_2$ + Fe + 4B in

262 the 25-900°C temperature range. Unindexed phases first appear at 560°C for α-phase and 690°C

263 for β-phase. (b) PXRD between the in-situ reaction's temperature range of 560-900°C. The red

264 triangles represent unindexed peaks for the unknown phase α and the yellow stars represent

265 unindexed peaks for the unknown phase β. (c) PXRD pattern, collected with Cu-Kα radiation, of

266 ternary $MgNi_3B_2$ produced due to the reaction of MgB_2 and Ni in salt flux. Minor phase peaks of

267 MgB_2 are represented by (*).

269 Partial mixing of elements may be achieved when binary MgB_2 is used as a source of boron

270 and magnesium. *Gillan et al.* have shown that the reaction of MgB_2 and metal chlorides may

271 produce corresponding binary metal borides, i.e., $MgB_2+FeCl_2 = MgCl_2+FeB$ [53]. The formation of

272 stable $MgCl_2$ was a thermodynamic driving force for this reaction. In our syntheses, the ternary

273 Mg-Fe boride was a target, so we attempted a reaction of MgB_2+Fe. Yet, MgB_2 is a relatively inert

14

274   precursor, and at temperatures of 750-850°C, the reaction of MgB_2 and elemental Fe is very slow,

275   presumably due to high kinetic activation barriers.

276   Hence, we attempted a hydride reaction using MgH_2 as a source of Mg. Unlike ductile Mg,

277   MgH_2 can be effectively mixed with Fe and B, and the released hydrogen may improve boron

278   reactivity. The hydride approach's success was demonstrated by synthesizing several compounds

279   in the Li-Ni-B system[39,40,54,55]. To guide hydride syntheses, we performed an in-situ powder X-ray

280   diffraction (PXRD) study (Fig. 9a). The formation of novel diffraction peaks which cannot be

281   assigned to known binary phases or elements in the Mg-Fe-B system was observed upon heating

282   in 560-820°C range. Unindexed peaks which do not match the α-$MgFeB_4$ calculated pattern appear

283   at 560°C (assigned as an α-unknown phase) and are present until 760°C (Fig. 9b).

284   Additionally, a set of second unknown peaks (assigned as β-unknown phase) formed at 690°C

285   and disappeared at 820°C. Upon further heating formation of FeB and FeSi was observed. An in-

286   situ study was performed in a sealed silica capillary that can react with Mg at high temperatures

287   as a Si source. Our in-situ study indicated that potential ternary phases had limited stability, and

288   reactions at temperatures above 820°C are expected to produce binary FeB. Our ex-situ hydride

289   reactions do not yield new phases in any appreciable amounts. Some possibilities for this could be

290   that the unknown phase incorporates silicon from the silica container, whereas for the ex-situ

291   reactions, niobium ampules are used for the reaction container. Another possibility is that this

292   phase is metastable, and the slower heating ramp in ex-situ reaction allows for this phase to

293   decompose.

294   The results above suggest that non-traditional solid-state methods may be required to

295   synthesize $MgFeB_4$. The two main challenges are the immiscibility of Mg and Fe and the upper

296   limit of ~820°C synthetic temperature, which is relatively low for borides. When Fe was replaced

297   with Ni, which is miscible with Mg, we were able to readily form a known ternary $MgNi_3B_2$ phase

298   (Fig. 9c). Further potential methods to produce target 114 borides discovered by the current

299   computational study include flux reactions and designing of special precursors with pre-built

300   functionality [56,57]. The latter approach was shown to be successful in the production of 1D B-P

301   polymeric chains [58]. Flux reactions need to be carefully designed to dissolve all consisting elements

302   (Mg, Fe, and B) yet not to react with container materials. Mg from flux readily reacts with silica,

303   while salt fluxes react with Nb or Ta ampoule materials at elevated temperatures. Further synthetic

304   explorations are currently underway.

Conclusion

In summary, using electronic structure calculations, we identified new structurally stable compounds among ternary borides of α-ATB4 type (A=Mg, Ca, Al; T=V, Cr, Mn, Fe, Ni, and Co). These predicted systems are characterized by numerous Van Hove singularities in their electronic spectrum formed by the emergence of highly localized quasimolecular states of 3d atomic dimers. Obtained VHS are stronger for electronic occupations near half filling of the 3d band and weaker for the states near the beginning and end of this band. The presence of such VHS, in turn creates favorable conditions for the development of different types of fluctuations and the appearance of new quantum states. In our case, we analyzed magnetic instabilities and found the formation of ladders of spin dimers in magnetic semiconducting (or weekly metallic) states that the experiment can verify. The systematic appearance of VHS as a function of the electronic population should be verified by spectroscopic experiments as these localized states are well separated by 1-2 eV. Overall, we demonstrated how to search for the systems with developing Van Hove singularities. The proposed variation of the type of 3d atoms represents a convenient tuning of the VHS strength, which can lead to instability of the original paramagnetic Fermi liquid and the formation of new magnetic states. While producing MgFeB4 experimentally was found to be challenging, we formulated a promising direction for further synthetic studies. The discovery of these materials would lead to an opportunity to study VHS systems and the possible formation of new quantum states including unusual magnetic orders, superconducting states, charge density waves and phase separation effects.

Methods

First-principles calculations. Density functional theory (DFT) calculations were carried out using the projector augmented wave (PAW) method[59] implemented in the VASP code[60,61]. The exchange and correlation energy is treated with the generalized gradient approximation (GGA) and parameterized by the Perdew-Burke-Ernzerhof formula (PBE)[62]. A plane-wave basis was used with a kinetic energy cutoff of 520 eV. The convergence criterion was set to 10^{-5} eV for the total energy and 0.01 eV/Å for ionic relaxation. Monkhorst−Pack's sampling scheme was adopted for Brillouin zone sampling with a k-point grid of $2\pi \times 0.033$ Å^{-1} for the structure optimization. Energy differences among different magnetic configurations and electronic density of states are computed

335 with a denser *k*-point grid of $2\pi \times 0.022$ Å^{-1}. Phonon calculations were performed with the density

336 functional perturbation theory[63] implemented in the VASP code and the Phonopy software[64].

337 **Phase stability calculations.** The phase stability is evaluated by the formation energy from spin-

338 polarized calculations. The formation energy E_f of ATB$_4$ is calculated as $E_f = E - \frac{1}{6}E(A) -$

339 $\frac{1}{6}E(T) - \frac{4}{6}E(B)$, where $E(M_x N_y B_z)$ is the total energy of bulk ATB$_4$. $E(A)$, $E(T)$ and $E(B)$ are

340 the total energies of A, T, and B ground-state bulk phases, respectively. E_d is defined by the

341 formation energy differences with respect to the three reference phases forming the Gibbs triangle

342 on the convex hull (If $E_d = 0$, it indicates the ATB$_4$ is a new stable phase, and the existing convex

343 hull should be updated. The reference phases in the convex hulls are obtained from the Material

344 Project database [38] and OQMD database [65].

345 **Electron-phonon coupling calculations.** The zone-center electron-phonon coupling (λ_Γ) was

346 calculated using the difference between the screened (ω) and unscreened ($\widetilde{\omega}$) zone-center phonon

347 frequencies [43] as

348
$$\lambda_\Gamma = \frac{\widetilde{\omega}^2 - \omega^2}{4\omega^2}. \tag{1}$$

349 The screened phonon frequency was computed by fully self-consistent (SC) calculations in the

350 displaced atomic configurations using the tetrahedron method with Blöchl corrections. To compute

351 the unscreened phonon frequency $\widetilde{\omega}$, the identical calculation was first performed in the

352 equilibrium configuration, followed by the calculations with the displaced atoms, but with partial

353 occupations fixed as the one in the equilibrium configuration. The detailed workflow of this

354 method can be found in[43].

355 **Synthesis.** For experimental synthetic attempts, MgB$_2$ powder (Alfa Aesar, 99%), Fe powder (JT

356 Baker, 99.5%), Cr powder (Alfa Aesar, 99.5%), Mn powder (Alfa Aesar, 99.95%), Ni powder

357 (Alfa Aesar, 99.996%), Co powder (Alfa Aesar, 99.998%), MgH$_2$ powder (Alfa Aesar, 99%),

358 MgCl$_2$ powder (Alfa Aesar, 99%), amorphous B powder (Alfa Asear, 98%), and Nb ampoules

359 were used. The total sample weight was 250 mg. A desired mixture of the ball-milled precursors

360 was loaded into Nb ampoule, which was weld-shut under Ar atmosphere in the glovebox. The

361 sealed Nb ampoules were enclosed in the Silica ampoule, which was evacuated and sealed using

362 the hydrogen-oxygen torch. Various reactions were attempted: the reaction of three elements

363 (Mg+Fe+4B), the reaction of magnesium boride with metal (2MgB$_2$+Fe), as well as hydride

364 reactions (MgH$_2$+Fe+4B). The typical heating profile consists of a 10-hour ramp up to the desired

temperature followed by isothermal annealing of 72 hours. After turning off the furnace, samples were allowed to cool back to room temperature.

Powder X-ray Diffraction (PXRD). After annealing, all samples were exposed to air and ground into fine powder using agate mortar. PXRD characterization was performed using Rigaku MiniFlex600 powder diffractometer with Cu-K_α radiation and Ni-K_β filter (λ= 1.54059 Å). *In-situ* PXRD was performed at beamline 17-BM at the Advanced Photon Source, Argonne National Laboratory (λ= 0.24110 Å). A mixture of MgH_2, Fe, and B in a 1.3:1:4 ratio was ball-milled and loaded into a silica capillary with a 0.5 mm inner diameter and 0.7mm outer diameter. The silica capillary was evacuated and flame-sealed such that the total length of the capillary was 50 mm. The capillary was placed vertically in a cell with resistive heating elements and aligned with the X-ray beam. Diffraction data were collected every 60 seconds as the sample was heated and cooled. Due to the reactor design, the thermocouple is slightly removed from the sample. We estimate that the error in the temperature is around 20-30°C. The reported temperature is the measured temperature.

Reference

1. Fleck, M., Oleś, A. M. & Hedin, L. Magnetic phases near the Van Hove singularity in s- and d-band Hubbard models. *Phys. Rev. B* **56**, 3159–3166 (1997).
2. González, J. Konh–Luttinger superconductivity in graphene. *Phys. Rev. B* **78**, 205431 (2008).
3. Kohn, W. & Luttinger, J. M. New mechanism for superconductivity. *Phys. Rev. Lett.* **15**, 524–526 (1965).
4. Rice, T. M. & Scott, G. K. New mechanism for a charge-density-wave instability. *Phys. Rev. Lett.* **35**, 120–123 (1975).
5. Van Hove, L. The occurrence of singularities in the elastic frequency distribution of a crystal. *Phys. Rev.* **89**, 1189–1193 (1953).
6. Li, G. *et al.* Observation of Van Hove singularities in twisted graphene layers. *Nat Phys* **6**, 109–113 (2010).
7. Cho, S. *et al.* Emergence of New van Hove Singularities in the Charge Density Wave State of a Topological Kagome Metal RbV3Sb5. *Phys Rev Lett* **127**, 236401 (2021).
8. Wu, S., Zhang, Z., Watanabe, K., Taniguchi, T. & Andrei, E. Y. Chern insulators, van Hove singularities and topological flat bands in magic-angle twisted bilayer graphene. *Nat Mater* **20**, 488–494 (2021).
9. Hu, Y. *et al.* Tunable topological Dirac surface states and van Hove singularities in kagome metal GdV$_6$Sn$_6$. *Sci Adv* **8**, (2022).
10. Wan, W., Harsh, R., Dreher, P., de Juan, F. & Ugeda, M. M. Superconducting dome by tuning through a van Hove singularity in a two-dimensional metal. *npj 2D Mater Appl* **7**, 41 (2023).

403 11. Dagotto, E., Nazarenko, A., Moreo, A., Haas, S. & Boninsegni, M. A simple theory for the
404   cuprates: the Antiferro-magnetic van Hove scenario. *Journal of Superconductivity* **8**, 483–
405   486 (1995).

406 12. Bok, J. & Bouvier, J. Van Hove Scenario for High T c Superconductors. in *High Tc
407   Superconductors and Related Transition Metal Oxides* 35–41 (Springer Berlin Heidelberg,
408   2007). doi:10.1007/978-3-540-71023-3_3.

409 13. Irkhin, V. Yu., Katanin, A. A. & Katsnelson, M. I. Effects of van Hove singularities on
410   magnetism and superconductivity in the t-t' Hubbard model: A parquet approach. *Phys Rev
411   B* **64**, 165107 (2001).

412 14. Goh, W. F. & Pickett, W. E. A mechanism for weak itinerant antiferromagnetism: Mirrored
413   van Hove singularities. *EPL (Europhysics Letters)* **116**, 27004 (2016).

414 15. Antropov, V. P. *et al.* On anomalies of anisotropic thermal expansion near points of
415   electronic topological transitions in noncubic metals. Applications to Zn, Cd and Cd-Mg
416   alloys. *Phys Lett A* **130**, 155–160 (1988).

417 16. Antropov, V. I. *et al.* Effect of proximity of the Fermi level to singular points in the band
418   structure on the kinetic and lattice properties of metals and alloys. *Soviet Physics Uspekhi*
419   **31**, 278 (1988).

420 17. Hicks, C. W. *et al.* Strong Increase of T_c of Sr_2RuO_4 Under Both Tensile and Compressive
421   Strain. *Science (1979)* **344**, 283–285 (2014).

422 18. Steppke, A. *et al.* Strong peak in T_c of $Sr_2 RuO_4$ under uniaxial pressure. *Science* **355**, (2017).

423 19. Barber, M. E., Gibbs, A. S., Maeno, Y., Mackenzie, A. P. & Hicks, C. W. Resistivity in the
424   Vicinity of a van Hove Singularity: Sr2RuO4 under Uniaxial Pressure. *Phys Rev Lett* **120**,
425   076602 (2018).

426 20. Liu, L. *et al.* Surface Van Hove Singularity Enabled Efficient Catalysis in Low-Dimensional
427   Systems: CO Oxidation and Hydrogen Evolution Reactions. *Journal of Physical Chemistry
428   Letters* **13**, 740–746 (2022).

429 21. Kuzma, Yu. B. Crystal structure of the compound YCrB4 and its analogs. *Sov. Phys.
430   Crystallogr.* **15**, 312 (1970).

431 22. Kuzma, Yu. B. New ternary Compounds with the structure of YCrB4 type. *Dopov. Akad.
432   Nauk Ukr. RSR Ser. A* **8**, 756–758 (1970).

433 23. Rogl, P. New ternary borides with YCrB4-type structure. *Mater Res Bull* **13**, 519–523
434   (1978).

435 24. Sobczak, R. & Rogl, P. Magnetic behavior of new ternary metal borides with YCrB4-type
436   structure. *J Solid State Chem* **27**, 343–348 (1979).

437 25. Veremchuk, I. *et al.* Synthesis, chemical bonding and physical properties of RERhB4
438   (RE=Y, Dy–Lu). *J Solid State Chem* **181**, 1983–1991 (2008).

439 26. Mori, T., Okada, S. & Kudou, K. Magnetic properties of thulium aluminoboride TmAlB4.
440   *J Appl Phys* **97**, 10A910 (2005).

441 27. Okada, S. *et al.* Properties of REAlB4 and Lu2AlB6 crystals grown from RE–Al–B
442   (RE=Tm, Yb, Lu) melts. *J Alloys Compd* **408–412**, 547–550 (2006).

443 28. Macaluso, R. T. *et al.* Crystal Structure and Physical Properties of Polymorphs of LnAlB 4
444   (Ln) Yb, Lu). *Chem. Mater.* **19**, 1918–1922 (2007).

445 29. Mori, T. *et al.* Crystal structure, chemical bonding, electrical transport, and magnetic
446   behavior of TmAlB4. *Phys Rev B* **76**, 064404 (2007).

447 30. Nakatsuji, S. *et al.* Superconductivity and quantum criticality in the heavy-fermion system
448   β-YbAlB4. *Nat Phys* **4**, 603–607 (2008).

449 31. Kuga, K., Karaki, Y., Matsumoto, Y., Machida, Y. & Nakatsuji, S. Superconducting
450   Properties of the Non-Fermi-Liquid System β−YbAlB. *Phys Rev Lett* **101**, 137004 (2008).
451 32. Dai, F., Feng, Z. & Zhou, Y. First principles investigation on mechanical and thermal
452   properties of α- and β-YAlB4 ultra-high temperature ceramics. *Journal of the American*
453   *Ceramic Society* **101**, 5694–5704 (2018).
454 33. Colón, Y. J. & Snurr, R. Q. High-throughput computational screening of metal–organic
455   frameworks. *Chem Soc Rev* **43**, 5735–5749 (2014).
456 34. Emery, A. A. & Wolverton, C. High-throughput DFT calculations of formation energy,
457   stability and oxygen vacancy formation energy of ABO3 perovskites. *Sci Data* **4**, 170153
458   (2017).
459 35. Sun, W. *et al.* A map of the inorganic ternary metal nitrides. *Nature Materials* **18**, 732–739
460   (2019).
461 36. Noh, J., Gu, G. H., Kim, S. & Jung, Y. Machine-enabled inverse design of inorganic solid
462   materials: promises and challenges. *Chem Sci* **11**, 4871–4881 (2020).
463 37. Yubuta, K. *et al.* Direct observation of the intergrown α-phase in β-TmAlB4 via high-
464   resolution electron microscopy. *Mater Res Bull* **44**, 1743–1746 (2009).
465 38. Jain, A. *et al.* Commentary: The Materials Project: A materials genome approach to
466   accelerating materials innovation. *APL Mater* **1**, 011002 (2013).
467 39. Gvozdetskyi, V. *et al.* Computationally Driven Discovery of a Family of Layered LiNiB
468   Polymorphs. *Angewandte Chemie - International Edition* **58**, 15855–15862 (2019).
469 40. Bhaskar, G. *et al.* Topochemical Deintercalation of Li from Layered LiNiB: toward 2D
470   MBene. *J Am Chem Soc* **143**, 4213–4223 (2021).
471 41. Slater, J. C. Magnetic Effects and the Hartree-Fock Equation. *Phys Rev* **82**, 538 (1951).
472 42. Nagamatsu, J., Nakagawa, N., Muranaka, T., Zenitani, Y. & Akimitsu, J. Superconductivity
473   at 39 K in magnesium diboride. *Nature* **410**, 63–64 (2001).
474 43. Sun, Y. *et al.* Electron-phonon coupling strength from *ab initio* frozen-phonon approach.
475   *Phys Rev Mater* **6**, 074801 (2022).
476 44. Wang, R. *et al.* High-Throughput Screening of Strong Electron–Phonon Couplings in
477   Ternary Metal Diborides. *Inorg Chem* **61**, 18154–18161 (2022).
478 45. Liu, A. Y., Mazin, I. I. & Kortus, J. Beyond Eliashberg Superconductivity in MgB2:
479   Anharmonicity, Two-Phonon Scattering, and Multiple Gaps. *Phys Rev Lett* **87**, 087005
480   (2001).
481 46. Devereaux, T. P., Cuk, T., Shen, Z. X. & Nagaosa, N. Anisotropic electron-phonon
482   interaction in the cuprates. *Phys Rev Lett* **93**, 117004 (2004).
483 47. Wang, R. *et al.* Theoretical prediction of a highly responsive material: Spin fluctuations and
484   superconductivity in FeNiB2 system. *Appl Phys Lett* **115**, 182601 (2019).
485 48. Akopov, G. *et al.* Synthesis-enabled exploration of chiral and polar multivalent quaternary
486   sulfides. *Chem Sci* **12**, 14718–14730 (2021).
487 49. Lee, S. J. *et al.* New Noncentrosymmetric Tetrel Pnictides Composed of Square-Planar
488   Gold(I) with Peculiar Bonding. *Chemistry – A European Journal* **27**, 7383–7390 (2021).
489 50. Akopov, G. *et al.* Third time's the charm: intricate non-centrosymmetric polymorphism in
490   LnSiP3 (Ln = La and Ce) induced by distortions of phosphorus square layers. *Dalton*
491   *Transactions* **50**, 6463–6476 (2021).
492 51. Lee, S. J. *et al.* Add a Pinch of Tetrel: The Transformation of a Centrosymmetric Metal into
493   a Nonsymmorphic and Chiral Semiconductor. *Chemistry – A European Journal* **28**,
494   e202104319 (2022).

495 52. Nayeb-Hashemi, A. A. & Clark, J. B. *Phase diagrams of binary magnesium alloys*. (ASM
496   International, 1988).
497 53. Abeysinghe, J. P., Kölln, A. F. & Gillan, E. G. Rapid and Energetic Solid-State Metathesis
498   Reactions for Iron, Cobalt, and Nickel Boride Formation and Their Investigation as
499   Bifunctional Water Splitting Electrocatalysts. *ACS Materials Au* **2**, 489–504 (2022).
500 54. Bhaskar, G. *et al.* Path Less Traveled: A Contemporary Twist on Synthesis and Traditional
501   Structure Solution of Metastable LiNi12B8. *ACS Materials Au* **2**, 614–625 (2022).
502 55. Gvozdetskyi, V. *et al.* A Hydride Route to Ternary Alkali Metal Borides: A Case Study of
503   Lithium Nickel Borides. *Chemistry – A European Journal* **25**, 4123–4135 (2019).
504 56. Kanatzidis, M. G., Pöttgen, R. & Jeitschko, W. The Metal Flux: A Preparative Tool for the
505   Exploration of Intermetallic Compounds. *Angewandte Chemie International Edition* **44**,
506   6996–7023 (2005).
507 57. Canfield, P. C. New materials physics. *Reports on Progress in Physics* **83**, 016501 (2019).
508 58. Woo, K. E., Wang, J., Mark, J. & Kovnir, K. Directing Boron-Phosphorus Bonds in
509   Crystalline Solid: Oxidative Polymerization of P=B=P Monomers into 1D Chains. *J Am
510   Chem Soc* **141**, 13017–13021 (2019).
511 59. Blöchl, P. E. Projector augmented-wave method. *Phys Rev B* **50**, 17953–17979 (1994).
512 60. Kresse, G. & Furthmüller, J. Efficiency of ab-initio total energy calculations for metals and
513   semiconductors using a plane-wave basis set. *Comput Mater Sci* **6**, 15–50 (1996).
514 61. Kresse, G. & Furthmüller, J. Efficient iterative schemes for ab initio total-energy
515   calculations using a plane-wave basis set. *Phys Rev B* **54**, 11169–11186 (1996).
516 62. Perdew, J. P., Burke, K. & Ernzerhof, M. Generalized Gradient Approximation Made
517   Simple. *Phys Rev Lett* **77**, 3865–3868 (1996).
518 63. Baroni, S., de Gironcoli, S., Dal Corso, A. & Giannozzi, P. Phonons and related crystal
519   properties from density-functional perturbation theory. *Rev Mod Phys* **73**, 515–562 (2001).
520 64. Togo, A. & Tanaka, I. First principles phonon calculations in materials science. *Scr Mater*
521   **108**, 1–5 (2015).
522 65. Kirklin, S. *et al.* The Open Quantum Materials Database (OQMD): assessing the accuracy
523   of DFT formation energies. *NPJ Comput Mater* **1**, 15010 (2015).
524
525

Acknowledgments

Competing Interests

The authors declare no competing interests.

Data Availability

The data used to support the findings of this study are available from the corresponding authors upon request.

Author Contributions

Y.S., K.K. and V.A. conceived the idea. Y.S. and Z.Z. performed calculations. A.P.P. and K.K. performed experiments. All authors contributed to data analysis and manuscript writing.